Delft University of Technology

Surface pressure reconstruction from LPT data with boundary conforming grids

Cakir, B.O.; Gonzalez Saiz, G.; Sciacchitano, A.

Important note
To cite this publication, please use the final published version (if applicable).
Please check the document version above.

Surface pressure reconstruction from LPT data with boundary conforming grids

Bora O Cakir[1,2,*] ⓘ, **Gabriel Gonzalez Saiz**[3] and **Andrea Sciacchitano**[3] ⓘ

[1] Turbomachinery and Propulsion Department, von Karman Institute for Fluid Dynamics, Rhode-Saint-Genèse, Belgium
[2] Department of Energy Sciences, Lund University, Lund, Sweden
[3] Faculty of Aerospace Engineering, Delft University of Technology, Delft, The Netherlands

E-mail: bora.orcun.cakir@vki.ac.be

CrossMark

Abstract

The coupling between fluid-structure interactions is governed by the pressure distribution over the interaction surface between the fluid and solid domains. The capabilities of non-intrusive optical techniques, such as particle image velocimetry and Lagrangian particle tracking (LPT), have been proven to provide accurate velocity and acceleration information within the flow field while simultaneously tracking the corresponding structural deformations. However, scattered data from LPT measurements are typically mapped onto Cartesian grids, independently of the shape of the solid objects in the measurement domain. The use of Cartesian grids poses challenges for the determination of the surface pressure because the velocity gradients close to the object's surface are not captured accurately. Therefore, an alternative surface pressure reconstruction scheme utilizing LPT data based on the arbitrary Lagrangian–Eulerian approach is proposed to mitigate the error propagation associated with the use of uniform grids. The introduced method provides an exact surface conformation utilizing boundary fitted coordinate systems and radial basis function based mesh deformations, which eliminates the need to use extrapolations to obtain surface pressure distributions. The introduced approach is assessed by means of a synthetic hill surface probing a three-dimensional analytical flow field; its practical applicability is demonstrated through an experimental characterization of turbulent boundary layer interactions with a steadily and unsteadily deforming elastic membrane.

Keywords: Lagrangian particle tracking, pressure reconstruction, fluid structure interaction, arbitrary Lagrangian Eulerian, boundary fitted coordinates

1. Introduction

The interaction mechanism between a fluid flow and a solid object comprises pressure and friction forces exerted on the solid object, with the former typically dominating over the latter. Moreover, in the case of non-rigid bodies, the pressure distribution is also responsible for the object deformation and, in turn, shape modifications. Hence, capturing pressure information within the flow field and over the object's surface is of primary importance. Several methods have been proposed to perform this task, which includes pitot tubes measuring pressure over prescribed locations within the measurement volume, orifices over the surface of experimental models acting as pressure taps, pressure transducers, and microphones determining the acoustic signals caused by the variations in

pressure fields (McKeon and Engler 2007). However, their capability to resolve instantaneous pressure distributions in the flow field or over surfaces is limited not only due to the intrusiveness of the measurement systems (Yu *et al* 2005) but also due to the sparsity of the measurements (being those point-wise measurement techniques). Additionally, evaluations of unsteady pressure fluctuations are restricted by the limited dynamic response of the measurement systems (Morris and Langari 2016). Considering the superiority of particle-image velocimetry (PIV) in terms of global non-intrusive velocity field determination and its broad spectrum of applicability (Westerweel *et al* 2013), a pressure reconstruction approach relying on the acquired velocity data and the flow governing equations proposes a great opportunity for obtaining simultaneous time-resolved velocity and pressure information in the entire measurement domain (van Oudheusden 2013).

### 1.1. Pressure from Lagrangian particle tracking (LPT)

Considering a fluid parcel, its material acceleration can be expressed using two different frameworks, namely the Eulerian and the Lagrangian approaches (Anderson *et al* 2020). Most studies on pressure field reconstruction from PIV data concur that higher accuracy is achieved when expressing material acceleration in the Lagrangian framework, specifically when the time scales of the flow are smaller than the temporal resolution of the experimental measurements (Huhn *et al* 2016, Pan *et al* 2016, Van Gent 2018). Accordingly, when particle tracking approaches (Maas *et al* 1993) are utilized, the reduction of material derivative computation errors by a factor of ∼2.5 is documented using a Lagrangian approach compared to PIV-based Eulerian approaches (Novara and Scarano 2012). Further developments in 3D-LPT methods enabled higher levels of accuracy, robustness and computational efficiency (Novara and Scarano 2013, Schanz *et al* 2016). Furthermore, the advent of helium-filled soap bubbles (HFSBs) as flow tracers has increased the measurement domain size of 3D-LPT experiments to the scale of cubic meters (Scarano *et al* 2015). Nevertheless, approaches aiming to increase the measurement spatial resolution beyond the inter-particle distance, which in large-scale experiments is often of the order of centimeters, need to be introduced (Gesemann *et al* 2016, Schneiders *et al* 2016, Cakir *et al* 2022).

With the availability of material acceleration information from the LPT/PTV data, the relation between velocity and pressure can be represented by the Navier–Stokes equation which provides the variation of pressure (∇p) over the measurement domain. Hence, the pressure field can be obtained by integrating the pressure gradients for which various approaches are being employed. Among these, spatially integrating the pressure gradients by means of solving a Poisson equation accompanied by the proper boundary conditions gained popularity due to its superior accuracy (Charonko *et al* 2010). Furthermore, Neeteson and Rival (2015) proposed a novel solution approach of utilizing Poisson equation for integration of pressure gradients on scattered Lagrangian domains by constructing a computational grid using Voronoi

tessellation (VOR) (Hirata 2005) and Delaunay triangulation (Blazek 2005). However, a comparative assessment of various pressure reconstruction techniques (van Gent *et al* 2017), demonstrated that the solution of the Poisson equation on gridded data yields the minimum pressure reconstruction errors with respect to a known ground truth. Moreover, the 3D B-spline particle track detection introduced by Gesemann *et al* (2016) for pressure determination-yielded root mean square (RMS) errors reaching ∼7% of the maximum pressure variation of the reference field, while VOR exceeded RMS error levels of ∼13%. Conversely, the pressure field computed over uniformly gridded data yielded RMS error levels bounded within ∼3%.

1.2. Surface pressure reconstruction

In fluid-structure interaction (FSI) problems, it is desirable to evaluate the static pressure over the surface of solid objects to determine the aerodynamic loads. There are two main methodologies to accomplish this task. One considers a control volume approach utilizing the momentum balance for which only the far field pressure information is required as a Dirichlet boundary condition (Oudheusden *et al* 2007, Ragni *et al* 2009, Mcclure and Yarusevych 2019). In this method, pressure computations over domains that contain intruding solid boundaries, are performed within regions which are not occupied by solid objects (de Kat and van Oudheusden 2012, Jeon *et al* 2018). However, this approach introduces large errors in the pressure estimation procedure owing to the significant dependency of the reconstruction process on the boundary conditions (Pan *et al* 2016). Moreover, the control volume approach does not provide any information regarding the distribution of aerodynamic loads over the surface of interest, rather the global aerodynamic loading on the objects only. The second approach is the calculation of the pressure distribution along the boundaries of the interaction interface by means of various extrapolation techniques (Murai *et al* 2007, Violato *et al* 2011, de Kat and van Oudheusden 2012). This reveals a broader spectrum of applicability as the overall loading yielded by the fluid is computed but also its local distribution is attained. Furthermore, following the immersed boundary treatment methods that define the fluid properties in Cartesian coordinate systems (Mittal and Iaccarino 2005, Shams *et al* 2015) proposed a ghost-cell approach that assigns fluid properties to the grid nodes inside the physical intrusions to satisfy the proper boundary conditions. Additionally, Jux *et al* (2020) proposed the employment of a partitioned domain by dividing the fluid domain into its rotational and irrotational regions. The pressure information over the irrotational domain is obtained by applying the Bernoulli equation, whereas a direct integration of the pressure gradients is performed within the rotational domain. The surface pressure is then computed considering smaller kernels of neighboring grid locations close to the surface of interest. Specific lines of integration are defined to relate the pressure gradient information omni-directionally between the already computed Cartesian grid locations and the surface boundary (Liu and Katz 2006). The method is applied
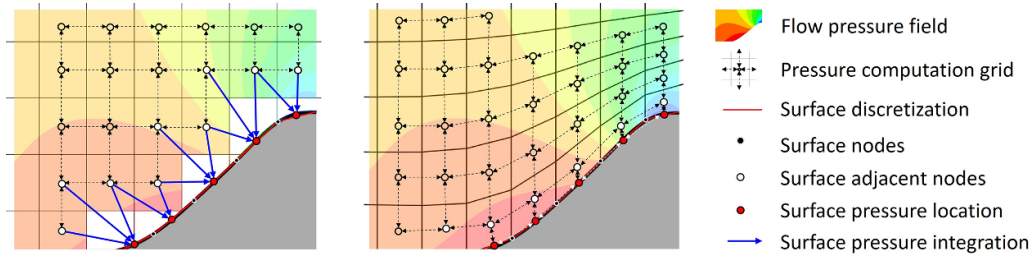
Figure 1. Surface pressure reconstruction via the Cartesian grid (left) and boundary fitted grid (right).

to reconstruct surface pressure over a 3D cyclist model and its capability of handling complex geometric contours intruding the flow field is demonstrated (Jux *et al* 2020). Finally, Pirnia *et al* (2020) employed a finite element approach for the computation of two-dimensional pressure information via integrating the pressure gradients using the Poisson equation. They proposed a cut-cell approach for handling immersed boundaries in which the integral form of the Poisson equation allows the proper definition of boundary conditions over the exact interface surfaces.

However, the use of omni-directional integration (ODI) approaches to recover pressure information extends beyond surface pressure reconstruction application. Liu *et al* (2016) proposed a new variation of the ODI approach with rotating parallel rays, which provides parallel integration paths for pressure gradients extending through the entire length of the fluid domain. Wang *et al* (2019) formulated a GPU-based version to significantly improve the computational efficiency, which was considered to be a critical disadvantage of the ODI approach, i.e. compared to solving the Poisson equation. Furthermore, a theoretical analysis of the error propagation characteristics for the ODI approach is provided, identifying key features for better pressure reconstruction accuracy by reducing the sensitivity to measurement noise (Liu and Moreto 2020). Subsequently, Liu and Moreto (2021) proposed a new implementation of the rotating parallel-ray ODI approach that allows pressure reconstruction around arbitrary shapes within multiply connected domains. Wang and Liu (2023) presented the Green's function integral (GFI) method, which is formulated similarly to ODI, but instead of a straight integration path, it performs integration along surfaces and volumes for 2D and 3D domains respectively and improves the computational efficiency via direct matrix inversion. Finally, another improvement in terms of reducing computational and memory requirements was introduced by Zigunov and Charonko (2024), who formulated the ODI approach as a matrix inversion problem that can match the efficiency of Poisson solvers.

Current pressure reconstruction schemes based on Poisson solvers perform integration of pressure gradients on uniformly structured computational grids. However, most practical engineering applications involve dynamic FSIs which contain curved solid boundaries that might deform unsteadily. Clearly, without a proper definition of the solid boundaries, the determination of surface flow properties (such as pressure,

wall shear stress, skin friction lines, etc.) becomes inaccurate or even impossible. More recently introduced methods for managing solid boundary intrusions separate the computational domain into multiple regions where close surface locations are handled by varying the integration direction for pressure reconstruction algorithms (figure 1, left). Although these methods provide accurate results in comparison to extrapolation techniques, they feature higher complexity and computational cost. Additionally, these algorithms do not account for the actual location, or even the motion, of the solid boundaries when computing the pressure distribution in the flow field. Therefore, in this work, an alternative approach to non-intrusive surface pressure reconstruction from LPT data over unsteadily deforming curved boundaries is introduced. The method developed based on the arbitrary Lagrangian-Eulerian (ALE) approach with boundary-fitted coordinate systems (figure 1, right) is detailed in section 2. Accuracy and resolution characteristics of the proposed approach are first quantified by means of a synthetic assessment where a Monte Carlo simulation-based uncertainty quantification is performed (section 3). Then, the applicability of the approach is demonstrated via an experiment reproducing the interaction between a turbulent boundary layer and a dynamically deforming elastic membrane (section 4).

2. Surface pressure reconstruction with boundary-fitted coordinates

The relationship between velocity and pressure can be established over the Navier–Stokes equations. Due to the higher accuracy with respect to the direct integration of the pressure gradients, the pressure field is then evaluated by solving the Poisson equation for pressure (Charonko *et al* 2010),

$$\nabla^2 p = \nabla \cdot (\nabla p) = \nabla \cdot \left(-\rho \frac{D\mathbf{u}}{Dt} + \mu \nabla^2 \mathbf{u} \right). \quad (1)$$

As referred to in equation (1), the pressure gradient is composed of two main components. The influence of the viscous terms is typically negligible for high Reynolds number flows (Murai *et al* 2007). Thus, the calculation of pressure gradients is dominated by the combination of spatial and temporal variations in particle velocity represented by $D\mathbf{u}/Dt$, which refers to the Lagrangian acceleration of a fluid particle (Voth *et al* 1998).
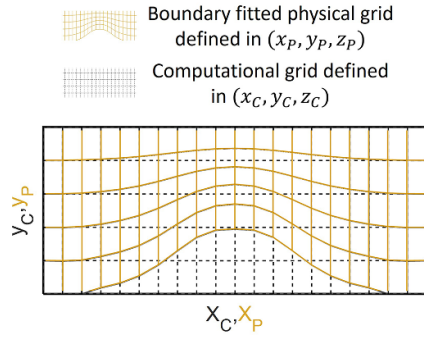
Figure 2. Computational and physical grid structures represented in the computational (x_C, y_C, z_C) and Cartesian (x_P, y_P, z_P) coordinate systems respectively.

2.1. The ALE method

In order to avoid the individual shortcomings of pure applications from Eulerian and Lagrangian perspectives while benefiting from their respective advantages, a technique referred to as the ALE method was introduced by Noh (1963) for numerical solution of hydrodynamic problems in the presence of unsteadily moving boundaries. Within the ALE formulation, the structural domain is analyzed with a Lagrangian method while the flow is characterized with an Eulerian description. The separate implementation of finite volume or difference methods for the fluid side and the finite element method for the structural domain allowed the numerical models to preserve their individual favorable properties for different kinematic behaviors of each domain (Hughes *et al* 1981).

2.2. Boundary-fitted coordinate systems

The generation of boundary-fitted coordinate systems for exact surface shape conformations is a common approach in computational fluid dynamics (CFDs). The implementation is used in a large variety of numerical algorithms as it allows the construction of a mesh structure that coincides with the boundary of the interacting domains. Thus, the relevant numerical discretizations of the integration and differentiation operators can be represented on these grids (Thompson *et al* 1985, Anderson *et al* 2020). The most important step of employing a boundary fitted grid is to establish a mapping function relating the computational coordinates, (x_C, y_C, z_C), to the Cartesian coordinates, (x_P, y_P, z_P) (figure 2). This task can be accomplished by employing an elliptic partial differential equation and solving the constructed equation for the coordinate variables of (x_C, y_C, z_C). Accordingly, the employed Laplace equation for the mesh generation is solved for each dimension individually in which the source terms P^i are employed to control the mesh specifications such as orientations and density of the grid lines by enforcing spatial resolution parameters,

$$\nabla^2 \psi^i = P^i \quad i = 1, 2, 3. \tag{2}$$

2.3. Unsteady mesh deformations

A possible approach to deal with unsteadily moving boundaries is to regenerate the body-fitted coordinates at the time step independently. However, this process generally requires a significant amount of user interaction to ensure that the mesh quality is not compromised and remains within the limits of the initially created form. Moreover, since the mesh must be updated at each time step in an unsteady or iterative manner, an efficient and reliable deformation method is necessary in terms of performance and computational efficiency. Therefore, an accurate grid deformation approach that does not alter drastically the initial mesh properties provides a valuable solution for unsteady simulations.

In this regard, the employment of radial basis functions (RBF) is well established in FSI applications as they are already utilized for schemes of information transfer over the fluid-structure interface where the matching of mesh locations is an exception (Smith *et al* 2000, Beckert and Wendland 2001). Their utilization for mesh deformation algorithms was first introduced by de Boer *et al* (2006, 2007) for which the mesh motion calculated on the boundary nodes by a point-by-point algorithm is interpolated in the internal domain using RBFs. Already with its first application, RBF-based mesh adaptation methods are shown to be able to generate high-quality mesh formations even in the case of large deformations. A high variety of RBFs are tested within this method, where Contour–Padé (CP) C^2 RBF with compact support is proven to be of the best performance with the choice of support radius appearing as an important factor for resultant mesh quality (Rendall and Allen 2010).

2.4. Pressure integration on boundary-fitted coordinates

The pressure gradients assigned to each computational grid location possess a physical orientation defined on the Cartesian coordinate system. However, in order to express the pressure gradients over the computational grid, the local transformation variables between the physical and computational grid formations are determined according to the vector transformation Jacobian ($\mathbf{J}_T$). Hence, the computational grid locations in any mesh form can be expressed as functions of the physical coordinates,

$$\begin{aligned}
x_C &= x_C (x_P, y_P, z_P) \\
y_C &= y_C (x_P, y_P, z_P) \\
z_C &= z_C (x_P, y_P, z_P)
\end{aligned} \tag{3}$$

where subscripts P and C, refer to the physical and computational coordinates respectively. Then, a transformation matrix ($\mathbf{T}$) is constructed to represent the information transfer between computational and physical coordinates.

$$\mathbf{T} = \frac{\partial\left(x_P, y_P, z_P\right)}{\partial\left(x_C, y_C, z_C\right)} = \begin{bmatrix} \frac{\partial x_P}{\partial x_C} & \frac{\partial x_P}{\partial y_C} & \frac{\partial x_P}{\partial z_C} \\ \frac{\partial y_P}{\partial x_C} & \frac{\partial y_P}{\partial y_C} & \frac{\partial y_P}{\partial z_C} \\ \frac{\partial z_P}{\partial x_C} & \frac{\partial z_P}{\partial y_C} & \frac{\partial z_P}{\partial z_C} \end{bmatrix}. \tag{4}$$

Thus, formulating the Poisson equation in the computational grid using the representation of the Laplacian operator

$$\nabla_C^2 p = \nabla_C^T \mathbf{I} \nabla p = \frac{1}{\mathbf{J_T}} \nabla_P^T \mathbf{I} \nabla_P p \tag{5}$$

as the gradient of pressure is represented by the material acceleration terms,

$$\nabla_C^2 p = \frac{1}{\mathbf{J_T}} \nabla_P^T \mathbf{I} \left(-\rho \frac{D\mathbf{u}}{Dt}\right). \tag{6}$$

Accordingly, an FFT-based Poisson solver with all Neumann boundary conditions can still be employed in consideration of a fully uniform structured formation of the computational grid (figure 2). Finally, as the pressure gradients are integrated over the computational grid, the resultant scalar variables of static pressure distribution do not necessitate any additional transformation between the computational and physical grids, so the pressure information possesses an exact one-to-one mapping between the two grids.

2.5. Implementation procedure

Depending on the measurement approach, the velocity and acceleration information can either be computed following an Eulerian approach or directly provided in terms of velocity and material accelerations (Shake-the-Box (STB) Schanz *et al* 2016). On the other hand, the motion of the structural surfaces is generally captured (figure 3, 1st stage) in terms of a Lagrangian approach where the surface motion is traced using various methods of surface tracers (Hwang *et al* 2007). After an initial boundary fitted grid structure is generated (figure 3, 2nd stage), the mesh is deformed according to the boundary motion so that the exact interaction between the fluid and solid domains can be expressed in a time-resolved manner (figure 3, 3rd stage). For each time instant, a transformation matrix is computed to allow accurate information transfer between the Cartesian grid and the boundary fitted computational grid. The velocity and material acceleration of the fluid domain is captured over a boundary fitted grid discretizing the measurement domain (figure 3, 4th stage). Finally, the integration of pressure gradients is performed using the Poisson equation (figure 3, 5th stage) constructed in equation (1) and solved using homogeneous Neumann boundary conditions at each face of the computational domain. Further details on the numerical implementation of the proposed approach including the mathematical background of the ALE approach, boundary fitted mesh generation and different RBFs were provided by Cakir (2020).

2.6. Pressure reconstruction via kernel integration

Throughout the synthetic and experimental assessments carried out to evaluate the boundary-adjusted surface pressure reconstruction approach, the authors have used an in-house
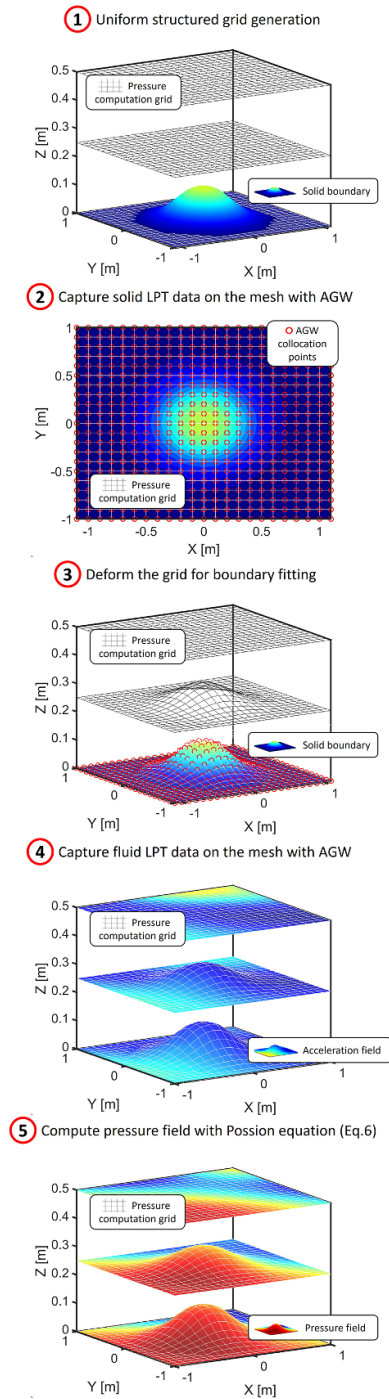
Figure 3. Surface pressure reconstruction procedure employing an arbitrary Lagrangian–Eulerian approach with boundary fitted grids.

developed kernel integration code inspired by Jux *et al* (2020) as a reference for comparison (figure 1, left). The implementation starts with a volumetric pressure reconstruction in the fluid domain, which is performed using a uniformly structured mesh with grid nodes penetrating the solid boundaries assigned to zero pressure gradients and an FFT-based solution of the Poisson equation is used with all Neumann boundary conditions. Then, for each solid boundary location discretized using the known structural shape or captured LPT information, a kernel of six fluid nodes is selected to ensure second-order
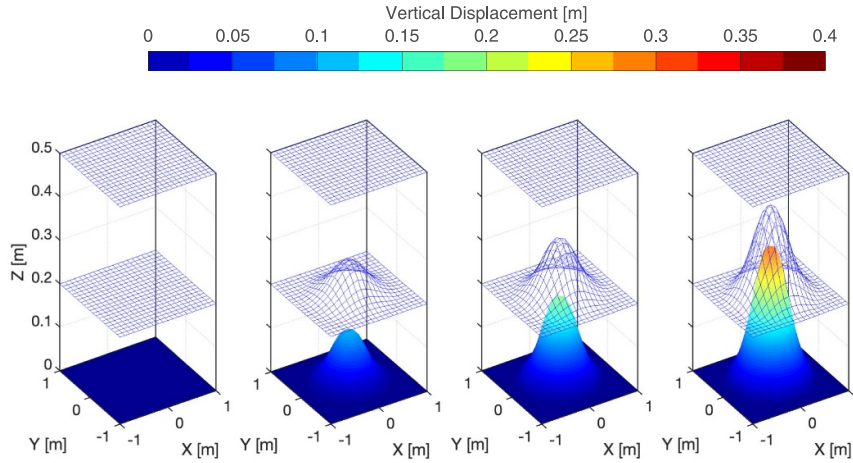
Figure 4. Surface deflections at different heights of the three-dimensional hill form and samples of horizontal planes for the corresponding deformed mesh structures.

numerical discretization in each direction. Using the fluid kernel and the material acceleration information associated with the structural node, a linear system of equations representing a local Poisson equation is constructed. Finally, the linear system (Poisson equation) is solved with known pressure values at the fluid nodes to obtain the surface pressure value. As explained above, the information transfer in this case is from the fluid to the structure, i.e. it is one-way, meaning that the pressure calculation within the fluid domain does not benefit from the shape and orientation of the solid boundary nor from the information about the physical motion of the membrane (velocity and acceleration).

3. Synthetic assessment

A synthetic assessment is performed using the exact 3D solutions of the unsteady incompressible Navier–Stokes equations defined by Ethier and Steinman (1994). Inspired by the 2D analytical solution provided for unsteady Navier–Stokes equations for Taylor-Green vortices (Taylor and Green 1937), they described a flow field in which the vorticity and the velocity vectors are parallel. The resultant flow field is referred to as a Beltrami flow (Wang 1990) and corresponds to a family of velocity and pressure fields whose unique determination is provided by the choice of constants *a, b, c, d* which satisfy $a^2 + b^2 = 0$ and $c = id$. In the case where *a* and *d* is selected to be arbitrary real numbers ($a = \pi/4$ and $d = \pi/2$), the flow field is computed via equation (7),

$$u = -a\left[e^{ax}\sin\left(ax \pm dz\right) + e^{az}\cos\left(ax \pm dy\right)\right]e^{-d^2 t}$$

$$v = -a\left[e^{ay}\sin\left(az \pm dx\right) + e^{ax}\cos\left(ay \pm dz\right)\right]e^{-d^2 t}$$

$$w = -a\left[e^{az}\sin\left(ax \pm dy\right) + e^{ay}\cos\left(az \pm dx\right)\right]e^{-d^2 t}$$

$$\begin{aligned}
p = -\frac{a^2}{2}&\left[e^{2ax} + e^{2ay} + e^{2az} + 2\sin\left(ax \pm dy\right)\right.\\
&\times\cos\left(az \pm dx\right)\mathrm{e}a\left(y + z\right)\\
&+ 2\sin\left(ay \pm dz\right)\cos\left(ax \pm dy\right)e^{a(z+x)}\\
&\left.+ 2\sin\left(az \pm dx\right)\cos\left(ay \pm dz\right)e^{a(x+y)}\right]e^{-d^2 t}.
\end{aligned} \quad (7)$$

For the pressure reconstruction procedure, the local and convective components of the acceleration terms are determined by analytically differentiating the velocity terms given above. As the computed material derivative terms are provided by the pressure reconstruction algorithm, the Poisson equation is solved with fully homogeneous boundary conditions, and the computed pressure field (which is unique up to a constant) is shifted according to an exact pressure value provided by equation (7). Furthermore, in order to test the surface pressure reconstruction algorithm with boundary fitted coordinates, an artificial three-dimensional hill forms with varying deformation amplitudes (from a flat surface, $h = 0$ m to $h = 0.1$ m, $h = 0.2$ m and $h = 0.3$ m) is introduced as a probing surface representing the intrusion of a solid boundary. Hence, an initially generated uniform grid structure is used to capture a discretized surface shape to generate the boundary-fitted coordinates which are deformed afterward according to the surface deflection levels (figure 4).

Furthermore, in order to simulate an experimental dataset of LPT, the theoretical flow field information is sampled at discrete scattered locations with a tracer particle concentration of $C = 80\text{par}/h_{\max}^3$ with the corresponding particle image densities over the projected volumes obtained as $N_P = 0.022$ ppp. The velocity and acceleration fields are computed at the time instant of $t = 0.5$ s based on the analytical formulation. The generated particles are propagated in seven time steps where the time separation between samples is set to $\Delta t = 10^{-3}$ s corresponding to an acquisition frequency of 1 kHz. The computed seven particle locations over the tracks are equipped with 0.2 voxels of Gaussian noise in each direction in order to simulate measurement and reconstruction noise (Sciacchitano *et al* 2022). Then, a Monte Carlo simulation (Metropolis and Ulam 1949) is performed with 100 samples according to the sampling criteria proposed by Schneiders and Sciacchitano (2017). The particle tracks are regularized with a polynomial fitting of second order from which the velocity and Lagrangian acceleration terms are calculated. Moreover, the acceleration information scattered over the computational domain is binned at the boundary of fitted grid nodes using AGW with spherical
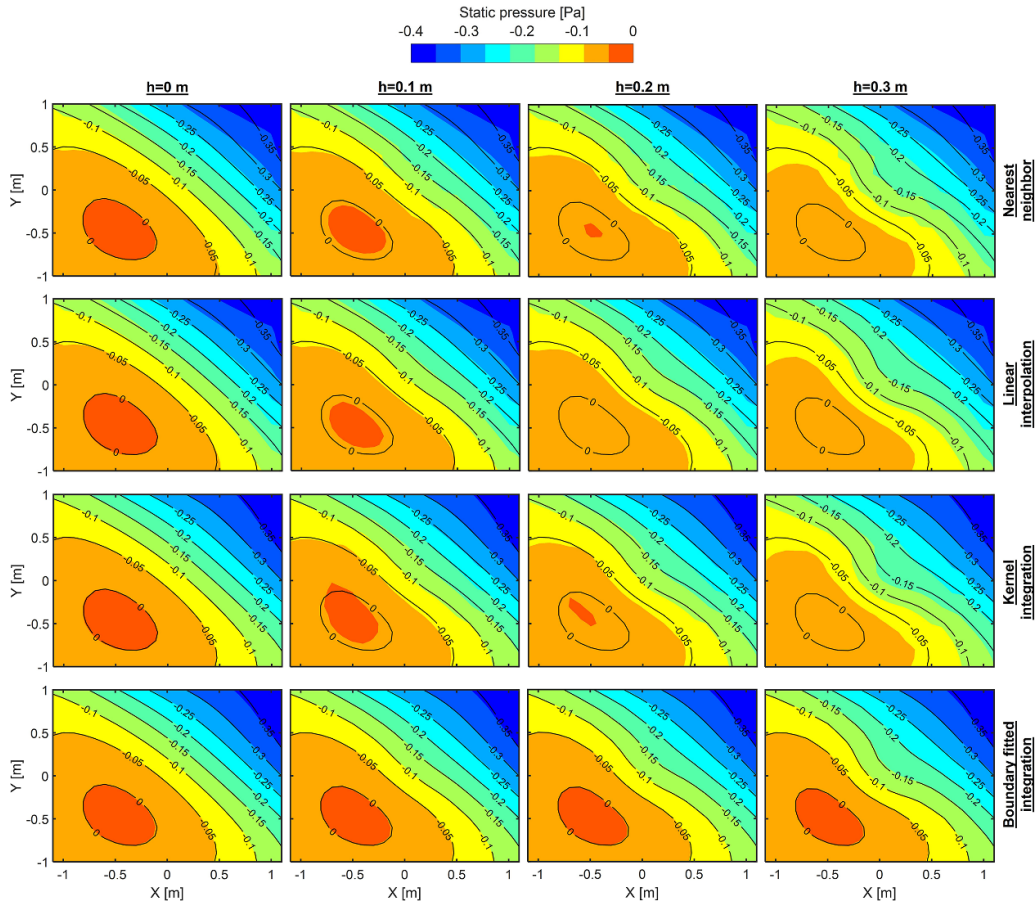
Figure 5. Surface pressure distributions over the 3D hill at maximum deflection levels of $h = 0$ m (1st column), $h = 0.1$ m (2nd column), $h = 0.2$ m (3rd column) and $h = 0.3$ m (4th column) reconstructed via the Cartesian grid and nearest neighbor (1st row), Cartesian grid and linear extrapolation (2nd row), Cartesian grid and kernel integration (3rd row) and boundary fitted grid (4th row). Color contours correspond to the reconstructed pressure with the aforementioned methods while the labeled contour lines correspond to the analytical pressure distribution.

bins of size $d_{AGW} = 0.2$ m which corresponds to ~50% overlaps between bins. The assigned acceleration information at the grid locations is transformed to switch from the physical coordinates of the boundary-fitted grid structure to the computational pressure integration mesh. For each iteration of the simulations, the resultant pressure fields from the reconstruction algorithm are compared with the analytical pressure field to extract the error distributions over the computational volume and the probing surface. The surface pressure distributions are also computed using a fully uniform structured grid and various extrapolation approaches of the nearest neighbor, linear extrapolation and kernel integration in order to demonstrate the improvements obtained with the proposed surface pressure reconstruction approach.

The first analysis is performed with the pressure reconstruction schemes applied to the case of zero surface deflection ($h = 0$ m). Since in this case there is no deformation, the boundary conforming grid also converges to the fully uniform structured grid and the transformation matrix yields a unity matrix for each grid location. Thus, as expected, there is no differ-

ence between various methods for surface pressure reconstruction, as both qualitative inspections (figure 5, 1st column) and the quantitative error extraction (figure 6) reveal identical results. Nonetheless, increasing the surface deflection level yield underestimations of the peak pressure values with all surface pressure prediction methods (nearest neighbor, linear extrapolation and kernel integration) that utilize a uniformly structured grid. This is due to the replacement of grid locations that are not associated with any acceleration information owing to the surface intrusion with zero pressure gradients. Hence, the pressure gradients in proximity to solid boundaries are underestimated, thus resulting in inaccurate surface pressure reconstructions.

While the nearest-neighbor and linear extrapolation approaches yield very similar outcomes, a slight accuracy improvement exists with linear extrapolation over the nearest-neighbor method at two deformation levels ($h = 0.1$ m and $h = 0.2$ m). This is influenced by to whether the surface collocation points over which the pressure is intended to be predicted overlap with the grid of the integration or not. In the case
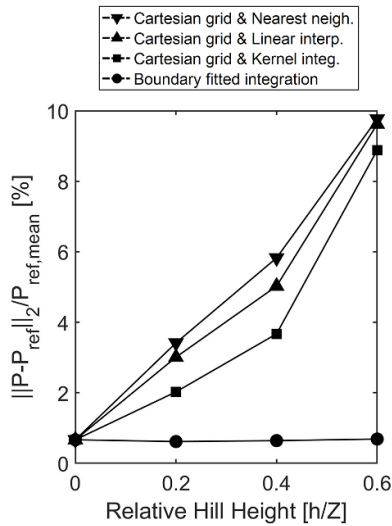
Figure 6. Variation of relative pressure reconstruction error with respect to the maximum surface deflection of the hill using different surface pressure reconstruction approaches.

of surface points that do not overlap, the linear extrapolation increases the degree of approximation by utilizing two nodes (hence a first order approximation) while the nearest neighbor approach uses the value of the closest node (remains as a zero-order approximation). In line with the aforementioned numerical order of discretization, the surface pressure integration approach utilizes the pressure gradients surrounding the specific surface node to construct a local Poisson problem which is used to integrate the pressure toward the surface of the solid object. Employing second-order finite differencing schemes, the resultant method is also of order two, which clearly relates to the improvement in reconstruction accuracy denoted by figure 5. Moreover, the fact that propagation of pressure information toward the surface relies on the physical constraints determined by the available pressure gradients within the measurement domain also contributes to the increasing accuracy of pressure reconstructions in comparison to the lower order methods.
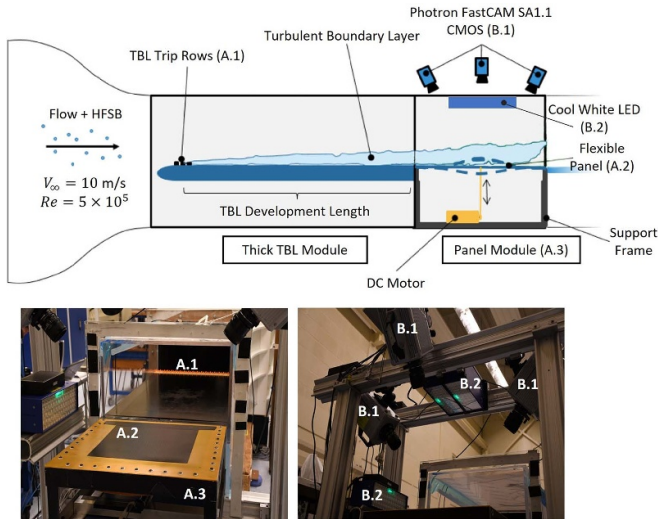
A local Poisson problem is constructed to compute the pressure distribution over the surface nodes using the kernel integration scheme. Hence, the pressure values computed using the uniform structured grid are provided for the linear system of equations with known variables. Thus, the influence of the underestimations in close proximity to the intruding surface boundary still persists, which relates to the similarities in the error variation with changing surface deflection levels in comparison to the nearest neighbor and linear extrapolation approaches. Therefore, the use of a conformal grid alleviates this issue by fitting the grid directly to the boundary. This allows all grid locations to be allocated with pressure gradient information. Hence, computation of the pressure field both within the measurement volume and over the membrane surface can be done with a single shot solution of the Poisson equation. Thus, with the use of boundary-fitted coordinates, a significant accuracy improvement is obtained

(figure 5, 4th row). Regardless of the respective hill height, the accuracy of the surface pressure reconstruction is preserved (figure 6). Since no nodes without pressure gradient information are assigned and no zero-pressure gradients are allocated over the course of the pressure integration grid, the underestimation of the pressure gradients toward the surface of the solid geometry is prevented. Even though there are inevitable numerical discretization errors associated with the ALE approach due to the construction of a transformation matrix, these are observed to be at a negligible level. On the other hand, the errors originated due to the absence of pressure gradient information for nodes that intrude through the surface, causing the reduction of reconstruction accuracy for methods that employ uniform grids.
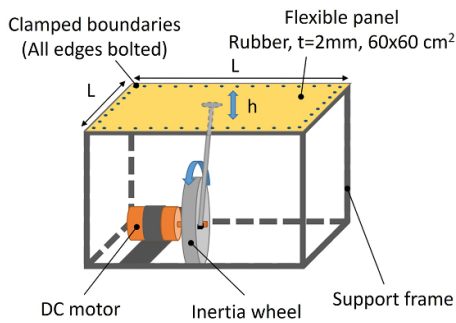
4. Experimental assessment

The experimental setup is designed with a square elastic membrane exposed to a turbulent boundary layer and equipped with a tomographic image acquisition system (figure 7). The elastic membrane is manufactured from 2 mm thick rubber. which is selected to have sufficiently high moment of inertia to prevent any aeroelastic deformations and have full control over the membrane shape. It has dimensions of $60 \times 60 \, \text{cm}^2$ and it is clamped on an aluminum frame of $60 \times 60 \times 30 \, \text{cm}^3$ from all edges to restrict its motion only to deformations. A DC motor is connected to the center of the membrane by means of a gear and rod mechanism and actuated at three different frequencies of 1 Hz, 3 Hz and 5 Hz with an amplitude of 40 mm from valley to crest (figure 8). The corresponding reduced frequencies ($k = \omega \times b/V_\infty$) obtained with the membrane motion of 1 Hz, 3 Hz and 5 Hz ($b = 0.25 \, \text{m} \, \& \, V_\infty = 12 \, \text{m s}^{-1}$) are $k_{1\text{Hz}} = 0.13$, $k_{3\text{Hz}} = 0.40$ and $k_{5\text{Hz}} = 0.65$ respectively. Hence, all shall be considered within the unsteady aerodynamics regime (Leishman 2016). Here, b represents the half chord length, which is considered to be the deformable side length of the membrane ($c = 0.5 \, \text{m}$). The translation of the central location of the membrane is defined as a cycle of vertical motion between the maximum and minimum deformation points. The measurements are performed with steady and unsteady membrane deformations. For the steady case, the flow is analyzed with the membrane at downward, neutral and upward positions.

A black foil with a regular grid of light-grey dots (0.8 mm diameter, 10 mm distance between adjacent dots, 36×36 dot grid) is applied to the upper face of the model to enable structural displacement measurements by means of LPT. A 120 cm long rigid plate is installed upstream of the model to ensure well-developed turbulent boundary conditions in the test section. The flow is seeded with neutrally-buoyant HFSB tracers, which are inserted into the flow via an in-house built seeding rake composed of 200 nozzles distributed over 12 wings. The LPT measurements are carried out via three Photron FastCAM SA1.1 CMOS cameras (1024 × 1024 pixels, 12-bit, 20 µm pixel sizes) mounted 40 cm above the moving panel positioned to form a 60° angle. Three cool white LED light sources are used for volumetric illumination

Figure 7. Schematic representation (top) and photos (bottom) of the experimental setup for turbulent boundary layer interactions with unsteadily deforming elastic membrane.

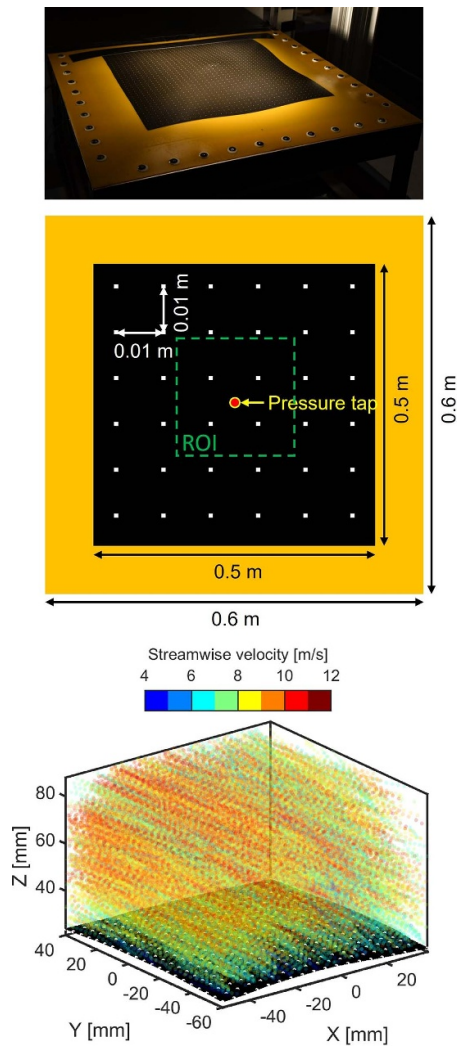**Figure 8.** Panel model and motion actuation system.

Table 1. Experimental setup and data processing parameters for the experimental investigation of turbulent boundary layer interactions with an unsteadily deforming elastic membrane.

Panel size ($L \times L$)	$60 \times 60\,\mathrm{cm}^2$
Panel thickness (t)	2 mm
Material	Rubber
Density	$1200\,\mathrm{kg\,m}^{-3}$
Young modulus (E)	0.05 GPa
Bending stiffness (EI)	$0.016\,\mathrm{N\,m}^2$
Amplitude motion (h)	20 mm
Freestream velocity	$12\,\mathrm{m\,s}^{-1}$
Reynolds number	$Re_l = 500\,000$
Boundary layer thickness	$\delta_{99} = 0.06\,\mathrm{m}$
Seeding	Helium filled soap bubbles
Seeding concentration	2×10^6 bubbles s^{-1}
Illumination	$3\times$LaVision LED-flashlight 300
Recording devices	$3\times$Photron FastCAM SA1.1 CMOS
Acquisition frequency	3000 Hz
Measurement volume	$20 \times 20 \times 15\,\mathrm{cm}^3$
Magnification	$M = 0.3$
Reconstructed track concentration	$C = 100\,\mathrm{par}/\delta_{99}^3$ ($N_p = 0.002\,\mathrm{ppp}$)
Track regularization	3rd order polynomial over 7 particles

4.1. Steady membrane deformations

The steady flow characteristics are investigated with the membrane stationarily deformed at three different locations: upward, neutral and downward. The steady membrane shape is reconstructed by combining the location information of surface markers obtained from the STB algorithm for 10 000 instantaneous fields. As the imaging range of recording devices allows accurate reconstruction of particle tracks for surface markers within a smaller area compared to the full size of the black foil, the membrane surface shape is represented by dimensions of $\sim 150 \times 150\,\mathrm{mm}^2$ (figure 9).

The steady flow field information of particle tracks is also treated in a very similar manner to the structural components as the instantaneous flow field information is combined from two consecutive runs with 10 000 time instants. The scattered particle tracking data is then gridded by means of a binning procedure (Aguera *et al* 2016) which proceeds with the following steps. First, a structured grid is generated for the membrane at neutral position where mismatches between the exact membrane locations and the grid nodes occur. Secondly, in order to confirm the various configurations of membrane surface shapes exactly, the initially generated structured grid shape is deformed by means of RBF-based mesh deformation schemes. Following the ALE approach, an Eulerian reference frame is created for the fluid side using the Lagrangian information captured by the structure. Then, spherical bins with diameter of $d_{\mathrm{AGW}} = 10\,\mathrm{mm}$ with 50% overlap are employed to capture particle tracks that will be used to reconstruct the fluid information over the measurement

of the flow and elastic membrane. The experimental setup is equipped with a TruStability™ HSC Series board mount pressure sensor (0.25% maximum error in output from a best fit straight line over the full-scale span), located at the central membrane location in order to provide reference static pressure values for comparisons against the results of non-intrusive surface pressure reconstruction algorithms.

The processing of raw images acquired is performed with the commercial software package DaVis version 10.0.5 from LaVision GmbH. To reconstruct the fluid motion, the acquired images are initially filtered using a Butterworth high-pass filter (Sciacchitano and Scarano 2014) computed over 15 images for cancellation of background reflections. The resultant images are then processed with the STB algorithm for LPT (Schanz *et al* 2016). The surface markers possess greater light intensities captured by the recording devices compared to the HFSB tracers of the fluid domain. Hence, in order to remove the flow tracers from the images, a high-pass time filter is applied to the recorded images with a filtering length of three images. The resultant images are processed with the STB algorithm employing the same minimum track length and degree of polynomial fitting with the fluid particles as indicated in table 1.

Figure 9. Photo and schematic representation of the elastic membrane utilized in the experimental campaign equipped with a black foil of regular gridded light-grey dots (top). Assembled STB data colored by the streamwise velocity and discretized membrane surface for the steady membrane deformation at the upward position (bottom).

domain. Finally, the AGW method is applied within each individual bin to three dimensions of velocity and acceleration vectors to assign the corresponding flow field information to the grid locations. Grid spacing for capturing the steady flow field information is defined to be 5 mm which corresponds to half of the separation distance between the surface markers. Hence, the location information of membrane shapes at the grid locations is supersampled by means of trilinear interpolation.

The reconstructed membrane shapes at different deformation levels of downward, neutral and upward positions are provided in figure 10. An important observation shall be made based on the deformation distribution which in turn affects the flow development over the membrane. By varying the cyclic displacement of the membrane central location, a 3D hill form is persistent for all three deformation stages. Since the region

of interest in the reconstruction of flow field properties is concentrated in proximity of the membrane center, the three stages of deformation yield a membrane shape that is displaced as a whole in the wall normal direction while the amplitude of the positive deflection (the hill height) varies. As it is provided in figure 10, the upward deformation stage has the maximum deflection level and the maximum elevation with respect to the downward position while the neutral position is in the middle, both in terms of elevation and deformation. This situation arises due to the plastic deformations of the elastic membrane experienced through multiple experimental campaigns. Accordingly, the membrane size extended beyond the initially aimed form. Hence, when clamped from the edges, a certain degree of sag is observed which causes the center of the membrane to always have a position deformation in comparison to its surroundings, preventing the intended cavity form to exist.

Starting with the streamwise velocity distributions shown in figure 11, it is observed that the flow remains fully attached to the membrane surface for all the surface deformation levels. The behavior of the flow through the measurement domain can easily be explained by following the law of mass conservation. As the membrane is deflected upward, the cross-section of the streamtube of the flow particles passing through the measurement domain is contracted, which requires the streamwise flow velocity to increase in order to satisfy continuity. Hence, with the upward deformation of the membrane in which the maximum surface elevation and deformation take place, the highest streamwise flow velocity magnitudes are obtained in comparison to the other deformation stages. A similar velocity profile also occurs for the membrane at the neutral position, but to the degree of lower magnitude of acceleration toward the central location of the membrane where the maximum deformation exits. At the downward deformation position of the membrane, no significant acceleration of the flow in the streamwise direction is present in comparison to the other stages of deformation as expected based on the correlation of the acceleration with the deformation amplitude.

The previously explained flow field behavior in terms of variations in the streamwise velocity component is related to the pressure gradients through the material acceleration terms in equation (1). Hence, within the direction of the positive flow acceleration, negative pressure gradients exist which suggests that there is an inverse relationship between the surface deformation levels and the local pressure distributions. Therefore, two main factors influence the range and profile of pressure distributions over the membrane surface at different deformation stages. First, the range of pressure values over the membrane between three different deformation levels reveals a decreasing trend from downward to upward levels. Hence, as the elevation level of the membrane within the region of interest is increased, the pressure values are reduced both over the entire membrane and the central location where the pressure tap is located. Secondly, as all deformation stages (downward, neutral and upward) yield a membrane shape that possesses positive deformation with a convex shape of the membrane in its central region, a similar profile of pressure distribution is persistent through the motion of the membrane.
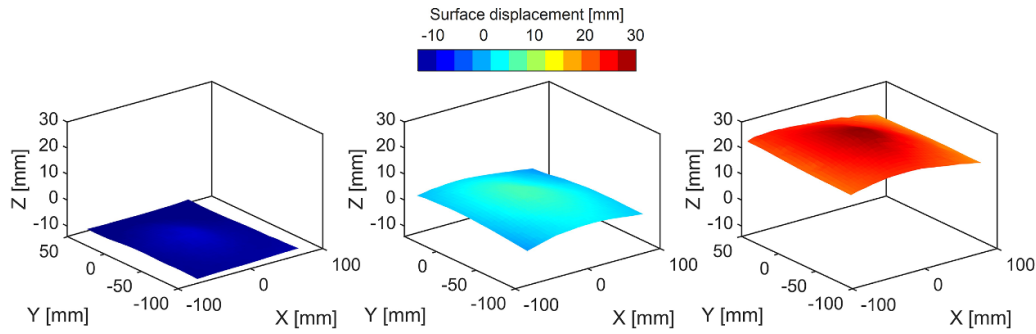
Figure 10. Reconstructed membrane shapes with surface displacements at downward, neutral and upward (left to right) deformed positions.
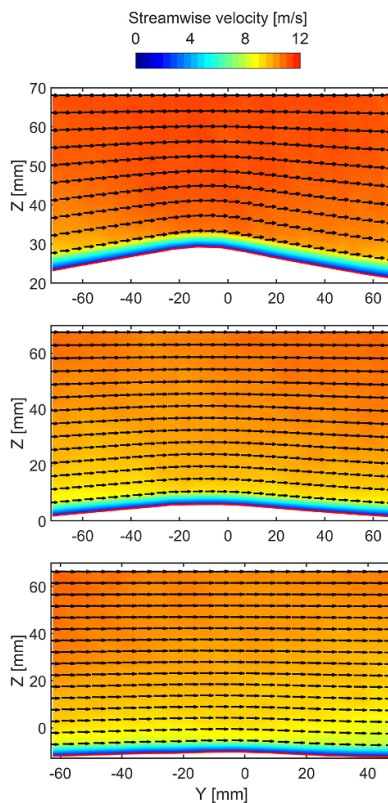

Figure 11. Streamwise velocity distributions at the central plane (X = 0 mm) of measurement volume for upward (top), neutral (middle) and downward (bottom) stages of deformation of the membrane.

This is associated with a correlation between positive deformation and positive local flow acceleration which is then related to the reduction of pressure toward the center of the membrane (figure 12).

The performance of various approaches for reconstruction of pressure distributions over the surface of the elastic membrane are investigated qualitatively based on the previously detailed flow behavior and quantitatively utilizing the pressure data acquired via the pressure tap at the central location of the membrane (table 2). For the downward stage of deformation, not only is the membrane at its lowest position but also the deformation variation over the membrane

surface is minimum. Hence, the variations between different methods of surface pressure reconstruction are also mitigated. As shown in the synthetic assessment, there is a direct correlation between the increasing surface deformation and the inaccuracy of surface pressure reconstruction utilizing the methods of nearest neighbor, linear extrapolation and kernel integration. Since these methods use the Cartesian grid to initially compute the pressure field information before propagating it toward the surface, the initial pressure computation grid is the main source of error. This is observed not to have a major impact on the membrane at the downward position. However, as the surface deformation is increased, underestimation of the central pressure value becomes apparent with the membrane at neutral position. While the surface pressure reconstruction with the conformal grid is able to maintain reconstruction accuracy, all the other methods slightly underestimated the pressure reduction toward the center.

Nonetheless, the differences between the various approaches can still be considered minimal since the error levels are well within the first decimal of the absolute pressure value measured by the pressure tap. Yet, an improvement over the nearest neighbor and linear interpolation approaches is already present with the use of the kernel integration method. This approach relies on physical constraints provided by pressure gradients and a second-order numerical discretization of the Laplacian of pressure that contributes to the mitigation of errors through a pressure integration procedure over the fully Cartesian grid. Finally, for the upward deformation state of the membrane, the differences between the selected approaches are amplified. While both nearest-neighbor and linear extrapolation methods yield error levels on the order of ~10%, this is reduced to ~1% with the use of kernel integration and conformal grid pressure reconstruction methods (table 3). Hence, the difference between the kernel integration and boundary fitted integration approaches is found to be significantly small. However, this is associated with the kernel integration overestimating the pressure variation within the wall normal direction due to the single-sided finite difference discretization of the local Poisson equation. Thus, the underestimation of the local pressure variation for fluidic nodes adjacent to the surface boundary is balanced out by the overestimation of the pressure gradients toward the surface,
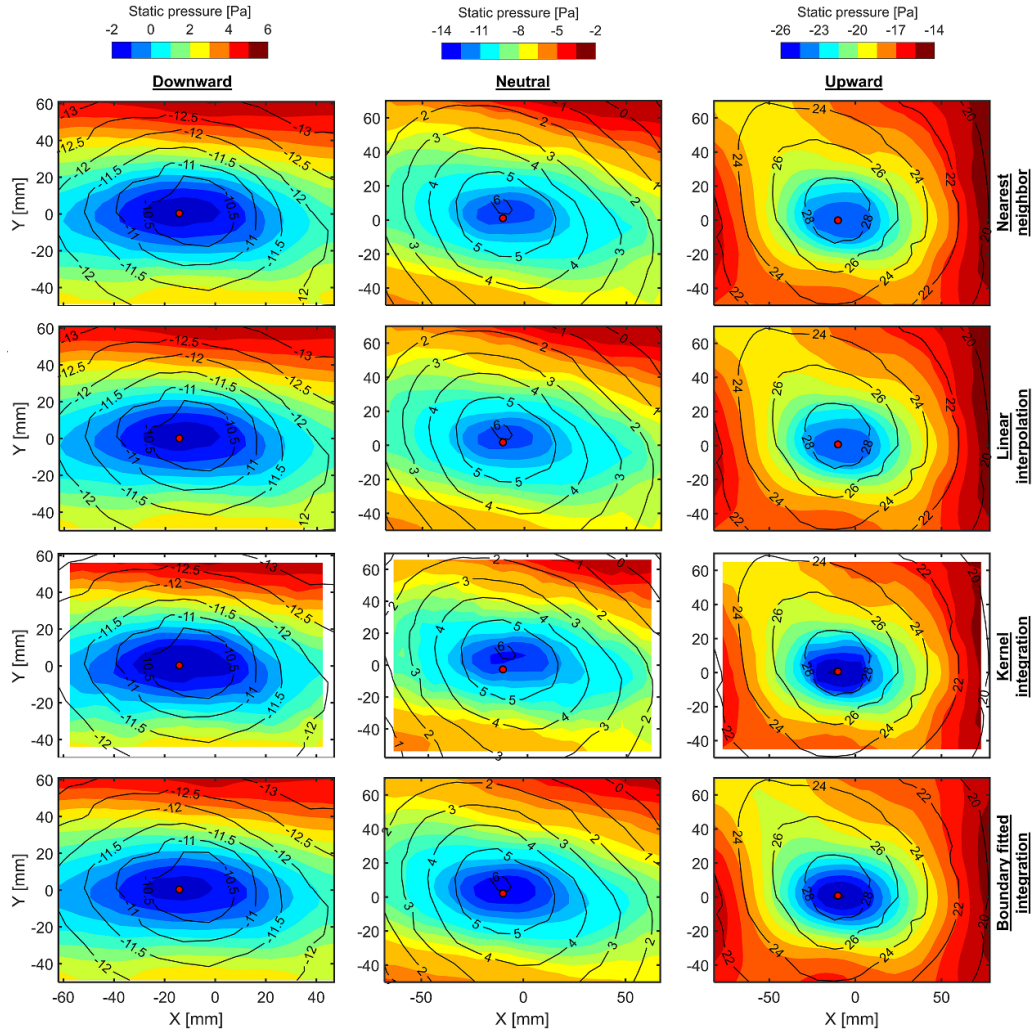
Figure 12. Surface pressure reconstruction via Cartesian grid and nearest neighbor (1st row), Cartesian grid and linear extrapolation (2nd row), Cartesian grid and kernel integration (3rd row) and boundary fitted grid (4th row) from STB data for membrane deformation levels of downward (1st column), neutral (2nd column) and upward (3rd column). Black contour lines with labels refer to the local distribution of membrane deformation levels in millimeters. Red dot indicates the pressure tap location.

Table 2. Static pressure [Pa] values at the central membrane location obtained from the pressure tap measurements and various surface pressure reconstruction approaches.

Deformation level	Pressure tap	NN	Lin. interp.	Kernel integ.	Boundary fitted
Upward	-25.89	-23.52	-23.53	-25.67	-25.77
Neutral	-10.83	-10.33	-10.32	-10.67	-10.98
Downward	-0.80	-1.21	-1.21	-1.26	-1.12

Table 3. Relative pressure reconstruction errors [%] at the central membrane (normalized with the pressure variation range of 26 Pa) location obtained from the various surface pressure reconstruction approaches with respect to the pressure tap measurements.

Deformation level	NN	Lin. interp.	Kernel integ.	Boundary fitted
Upward	9.2%	9.2%	1.1%	1.0%
Neutral	2%	2%	0.6%	0.6%
Downward	1.6%	1.6%	1.7%	1.2%

both due to the surface boundary not being incorporated in the process of reconstructing pressure over the flow field parcels.

4.2. Unsteady membrane deformations

The phase-averaged flow field data for the unsteady membrane motion is captured following a similar procedure applied to the steady case. For each phase of the membrane motion, multiple time instants ($[t_0 - \alpha \Delta t, t_0 + \alpha \Delta t]$) are ensemble averaged

employing where $\Delta t = 1/3000$ seconds and t_0 are the time instant of the phase. In order to ensure that the validity of the unsteady terms is preserved (material acceleration information captured via STB), the coefficient α is varied for different actuation frequencies ($\alpha_{1\,Hz} > \alpha_{3\,Hz} > \alpha_{5\,Hz}$). Depending on the prescribed time intervals, phases of $\Delta T = 2\alpha \Delta t = T/20$ time duration are determined for the particle track information to be combined, in which T corresponds to the time duration
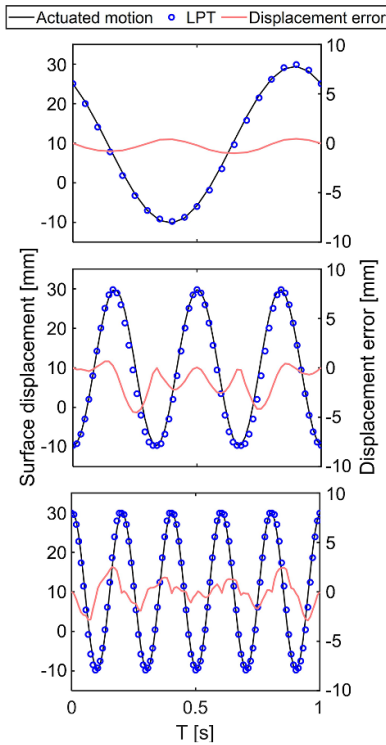
Figure 13. Surface displacement level and reconstruction error of membrane central location captured via the LPT measurement system vs actuated motion by means of the DC motor-rod mechanism for actuation frequencies of 1 Hz (top), 3 Hz (middle) and 5 Hz (bottom).

Figure 14. Number of particles captured over the central location of the membrane at upward deformation position for steady (left) and unsteady (right) motion of the membrane as an ensemble of STB output.

of a period of cyclic motion of the membrane. The instantaneous reconstruction of the membrane shape is possible via the measurement of the locations of the surface markers. Surface markers are tracked via the LPT system and the STB algorithm is employed to reconstruct the membrane shape and deformation level both for steady (figure 10) and unsteady (figure 13) actuations. In order to quantify the accuracy of the structural motion reconstruction, the deformation of the central location of the membrane captured via the optical measurement setup is compared against the known actuation at the pressure tap location. Accordingly, figure 13 shows the comparison of measured and induced motion at three different frequencies (1 Hz, 3 Hz and 5 Hz). The RMS error levels of the membrane central position over the actuated motion are below $\sim$0.8, $\sim$0.9 and $\sim$0.8 mm, respectively.

Utilizing the surface deformation captured by the STB algorithm, the computational domain is created starting from a uniformly structured grid and deforming the generated mesh using the RBF-based mesh deformations based on the location information of the membrane surface makers. Then, the combined particle tracks containing particle velocity and acceleration data are binned over the deformed grid locations. In comparison to the flow field reconstructions over the steady deformation of the elastic membrane, the resolution of the grid generated for capturing the flow field information is reduced

and the bin size for the AGW method is doubled (figure 14). As the temporal window ($2\alpha\Delta T$) reduces with increasing frequency of membrane actuation (in order to ensure validity of the quasi-steady assumption), the corresponding number of particle tracks captured within the bins is also reduced with increasing frequency (figure 14, right).

Analyzing the performance of different surface pressure reconstruction approaches for capturing the surface pressure distributions over the unsteadily deforming elastic membrane, the pressure value at the membrane's central position is again compared with the pressure tap readings at the same position. Accordingly, the nearest neighbor and linear extrapolation approaches are observed to yield almost completely identical results for all actuation frequencies (figure 15). These two methods are expected to have unnoticeable small differences based on the results of the pressure reconstructions performed for the steady membrane deformation case. This expectation is associated with the fact that the elastic membrane exhibits relatively small deformation levels over the membrane surface in comparison to the synthetic assessment. Thus, the distance between the membrane and the adjacent nodes is relatively small, which reduces the impact of the first order approximation ($y = ax+b$), causing the solution of the linear extrapolation to approach that of the nearest-neighbor method. On the other hand, the kernel integration approach is observed to improve the accuracy of the pressure reconstructions significantly while the best results over the cycle of the membrane motion are obtained with the proposed boundary fitted integration method (figure 15). However, the overall profile of the pressure variation over the entire cycle of the membrane motion is observed to be consistently well captured by all the methods and the RMS of error values yield relatively similar reconstruction accuracy metrics. Nonetheless, quantitatively, the error values are reduced from $\sim$10% to $\sim$5% with the use of kernel integration and to $\sim$3% with the use of boundary fitted integration (table 4).
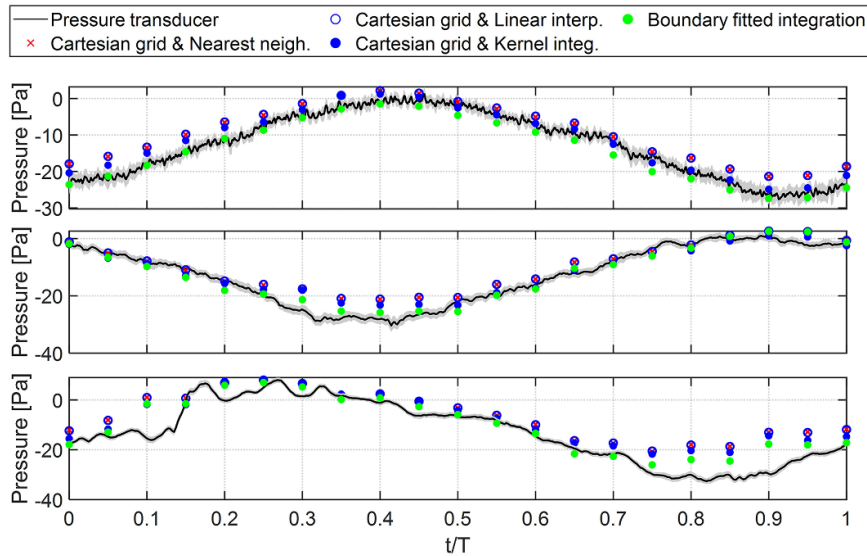
Figure 15. Phase-averaged pressure reconstruction via nearest-neighbor, linear extrapolation, kernel integration and boundary-fitted integration methods in comparison to the pressure tap measurements for 1 Hz (top), 3 Hz (middle) and 5 Hz (bottom) of unsteady membrane motion.

Table 4. RMS of instantaneous pressure reconstruction errors [Pa] of nearest-neighbor, linear extrapolation, kernel integration and boundary-fitted integration methods for 1 Hz, 3 Hz and 5 Hz of unsteady membrane motion.

	Motion frequency		
	1 Hz	3 Hz	5 Hz
NN	2.48	3.52	7.81
Lin. interp.	2.48	3.52	7.81
Kernel integ.	1.55	2.37	5.62
Boundary fitted	1.02	2.12	5.01

Referring to the two main aspects of the time evolution of pressure values at the central membrane location, the theoretical assumption of zero normal pressure gradients within the turbulent boundary layer is observed to have a superior effect for determining the amplitude of pressure variations. The reference pressure value is computed at the edge of the boundary layer over the temporal trace of velocity values. This provided 70% of the pressure variation amplitudes throughout the motion cycle of the membrane. Since this changes the flow velocity well outside the boundary layers, which is used as a Dirichlet boundary condition for the pressure reconstruction scheme, the impact of the pressure integration method is already significantly alleviated. Accordingly, the integration of the pressure gradients composed the 30% of the total pressure variation over the cyclic motion of the membrane. Hence, a significantly good agreement with the pressure tap measurements is obtained regardless of the reconstruction technique (figure 15). Secondly, as the membrane goes through cyclic motion, the captured phases contain the membrane deformed at upward, neutral and downward positions. Among these, the highest degree of difference between the different surface pressure integration approaches occurs for the upward deformation position where the maximum level

of displacement variation over the surface of the elastic membrane exists. However, as the error values are averaged over the entire cycle of the membrane motion, the overall RMS value is suppressed by the reconstruction error computed for the membrane at phases of lower deformation levels. Finally, even in the case of 5 Hz of membrane motion frequency where mechanical vibrations of the structural housing were observed, the reconstructed pressure values are captured in close agreement with the pressure tap measurements. Nevertheless, it should be noted that the pressure tap measurements at 5 Hz membrane motion frequency do suffer from larger measurement uncertainties caused by the greater vibration amplitudes induced, especially at the upward deformation boundary, due to the high impact forces of membranes on the aluminum housing.

5. Conclusions

The physical description of FSIs demands surface loading over the structural elements to be determined according to the surrounding flow field. In this regard, optical measurement techniques such as PIV/LPT enable non-intrusive characterization of flow field properties in proximity to a solid object, including velocity and acceleration information, as well as tracking the motion of solid boundaries. Nevertheless, as surface deformations occur in response to aerodynamic loads, the most critical information that needs to be extracted is the pressure distribution over the solid boundaries. Although various approaches previously employed for this purpose exist, the surface information so far has not been integrated in the fluid domain, with Cartesian meshes typically being employed for the description of the flow properties. This causes the error propagation through pressure reconstruction to deteriorate the performance of these approaches. Accordingly, an alternative surface

pressure reconstruction scheme based on LPT data is proposed based on the ALE approach. The introduced approached employed boundary-fitted coordinate systems generated by means of RBF-based mesh deformations to achieve perfect solid boundary conformation. Therefore, the exact conformation of the deformed surface shapes eliminates the necessity of any extrapolation method for surface pressure distribution determination.

The proposed approach is first tested on a synthetic dataset against conventional surface pressure reconstruction schemes for nearest neighbor, linear extrapolation and kernel integration. While all methods converge to the same solution for a measurement domain with no solid boundary intrusions, approaches that utilize a fully uniform structured grid for the initial computation of the pressure field within the measurement domain are observed to yield errors with increasing amplitude as the surface intrusion is amplified. Contrarily, the proposed boundary fitted pressure reconstruction approach is shown to preserve high accuracy of surface pressure reconstructions through all levels of surface deformations. Furthermore, the proposed approach is utilized to perform surface pressure reconstructions over an elastic membrane that is deformed in a controlled manner to investigate turbulent boundary layer interactions with deforming solid bodies. The improvements obtained with the introduced approach were clearly demonstrated with the static membrane deformation where for the maximum deformation stage, an error of pressure reconstruction reduction from ∼10% to ∼3% is documented. For the unsteady membrane deformations in which the error values are being suppressed due to the existence of time instants during which no significant surface deformation is captured, the highest accuracy of surface pressure reconstruction is obtained with the boundary-fitted pressure integration method reducing with up to a factor of 2.5 with respect to state-of-the-art extrapolation approaches.

Although the proposed method is assessed with relatively simple geometries of three-dimensional hill forms, the approach is applicable to objects of a wide range of geometries. In particular, when extended to unstructured meshes, which can enable higher accuracy of surface conformations, the limitations originating from geometric complexity can be easily mitigated. Since the presented approach utilizes material acceleration information directly available from LPT, the binning process can be employed over any mesh structure regardless of formation strategy, which enables meshes that prioritize better surface representation to be opted for. Moreover, with the incorporation of mesh deformations based on the structural motion, the selected RBF-based schemes ensure highly accurate numerical discretization which enable accurate surface pressure determination via the solution of the Poisson equation. Finally, the coordinate transformation process is suitable for any arbitrary mesh formation as it relies on numerical discretization between the meshes through derivatives. Thus, the method has the potential to be applied for surface pressure reconstructions around complex objects of arbitrarily complex shapes.

Data availability statement

All data that support the findings of this study are included within the article (and any supplementary files).

ORCID iDs

Bora O Cakir ⬡ https://orcid.org/0000-0002-3577-4730
Andrea Sciacchitano ⬡ https://orcid.org/0000-0003-4627-3787

References

Agüera N, Cafiero G, Astarita T and Discetti S 2016 Ensemble 3D PTV for high resolution turbulent statistics *Meas. Sci. Technol.* **27** 124011

Anderson D *et al* 2020 *Computational Fluid Mechanics and Heat Transfer* 4th edn (CRC Press)

Beckert A and Wendland H 2001 Multivariate interpolation for fluid-structure-interaction problems using radial basis functions *Aerosp. Sci. Technol.* **5** 125–34

Blazek J 2005 Principles of grid generation *Computational Fluid Dynamics: Principles and Applications* 2nd edn, ed J Blazek (Elsevier Science) ch 11, pp 373–413

Cakir B O 2020 Bridging experimental simulations with computational frameworks for time-resolved characterization of fluid-structure interactions *Master's Thesis* Delft University of Technology

Cakir B O, Gonzalez Saiz G, Sciacchitano A and van Oudheusden B 2022 Dense interpolations of LPT data in the presence of generic solid objects *Meas. Sci. Technol.* **33** 124009

Charonko J J, King C V, Smith B L and Vlachos P P 2010 Assessment of pressure field calculations from particle image velocimetry measurements *Meas. Sci. Technol.* **21** 105401

de Boer A, der Schoot V and Bijl H 2006 New method for mesh moving based on radial basis function interpolation *ECCOMAS CFD 2006: Proc. European Conf. on Computational Fluid Dynamics*

de Boer A, van der Schoot M and Bijl H 2007 Mesh deformation based on radial basis function interpolation *Comput. Struct.* **85** 784–95

de Kat R and van Oudheusden B W 2012 Instantaneous planar pressure determination from PIV in turbulent flow *Exp. Fluids* **52** 1089–106

Ethier C R and Steinman D A 1994 Exact fully 3D Navier-Stokes solutions for benchmarking *Int. J. Numer. Methods Fluids* **19** 369–75

Gesemann S *et al* 2016 From noisy particle tracks to velocity, acceleration and pressure fields using B-splines and penalties *18th Int. Symp. on Applications of Laser Techniques to Fluid Mechanics proc.*

Hirata T 2005 3-D Voronoi tessellation algorithms *Jpn. J. Ind. Appl. Math.* **22** 223

Hughes T J, Liu W K and Zimmermann T K 1981 Lagrangian-Eulerian finite element formulation for incompressible viscous flows *Comput. Methods Appl. Mech. Eng.* **29** 329–49

Huhn F, Schanz D, Gesemann S and Schröder A 2016 FFT integration of instantaneous 3D pressure gradient fields measured by Lagrangian particle tracking in turbulent flows *Exp. Fluids* **57** 151

Hwang T, Doh D, Jo H, Tsubokura M, Piao B, Kuroda S, Kobayashi T, Tanaka K and Takei M 2007 Analysis of fluid-elastic-structure interactions in an impinging jet with a

dynamic 3D-PTV and non-contact 6D-motion tracking system *Chem. Eng. J.* **130** 153–64

Jeon Y, Gomit G, Earl T, Chatellier L and David L 2018 Sequential least-square reconstruction of instantaneous pressure field around a body from TR-PIV *Exp. Fluids* **59** 27

Jux C, Sciacchitano A and Scarano F 2020 *Flow Pressure Evaluation on Generic Surfaces by Robotic Volumetric ptv* (Measurement Science and Technology)

Leishman J 2016 *Principles of Helicopter Aerodynamics* (*Cambridge Aerospace Series*) (Cambridge University Press) (available at: https://books.google.com.tr/books?id = uscAMQAACAAJ) p 360

Liu X and Katz J 2006 Instantaneous pressure and material acceleration measurements using a four-exposure PIV system *Exp. Fluids* **41** 227

Liu X and Moreto J R 2020 Error propagation from the PIV-based pressure gradient to the integrated pressure by the omnidirectional integration method *Meas. Sci. Technol.* **31** 055301

Liu XMoreto J R 2021 Pressure reconstruction of a planar turbulent flow field within a multiply connected domain with arbitrary boundary shapes *Phys. Fluids* **33** 101703

Liu X, Moreto J R and Siddle-Mitchell S 2016 Instantaneous pressure reconstruction from measured pressure gradient using rotating parallel Ray method *AIAA* (https://doi.org/10.2514/6. 2016-1049)

Maas H G, Gruen A and Papantoniou D 1993 Particle tracking velocimetry in three-dimensional flows *Exp. Fluids* **15** 133–46

Mcclure J and Yarusevych S 2019 Planar momentum balance in three-dimensional flows: applications to load estimation *Exp. Fluids* **60** 41

McKeon B and Engler R 2007 *Pressure Measurement Systems* (Springer) pp 179–214

Metropolis N and Ulam S 1949 The Monte Carlo method *J. Am. Stat. Assoc.* **44** 335–41

Mittal R and Iaccarino G 2005 Immersed boundary methods *Annu. Rev. Fluid Mech.* **37** 239–61

Morris A S and Langari R 2016 Pressure measurement *Measurement and Instrumentation* 2nd edn, ed A S Morris and R Langari (Academic) pp 463–91

Murai Y, Nakada T, Suzuki T and Yamamoto F 2007 Particle tracking velocimetry applied to estimate the pressure field around a Savonius turbine *Meas. Sci. Technol.* **18** 2491–503

Neeteson N J and Rival D E 2015 Pressure-field extraction on unstructured flow data using a voronoi tessellation-based networking algorithm: a proof-of-principle study *Exp. Fluids* **56** 44

Noh W F 1963 Cel: a time-dependent, two-space-dimensional, coupled eulerian-lagrange code (https://doi.org/10.2172/ 4621975)

Novara M and Scarano F 2012 Lagrangian acceleration evaluation for tomographic PIV: a particle-tracking based approach *16th Int Symp. on Applications of Laser Techniques to Fluid Mechanics* (*Lisbon, Portugal*)

Novara M and Scarano F 2013 A particle-tracking approach for accurate material derivative measurements with tomographic PIV *Exp. Fluids* **54** 1584

Oudheusden B *et al* 2007 Evaluation of integral forces and pressure fields from planar velocimetry data for incompressible and compressible flows *Exp. Fluids* **43** 153–62

Pan Z, Whitehead J, Thomson S and Truscott T 2016 Error propagation dynamics of PIV-based pressure field calculations: how well does the pressure Poisson solver perform inherently? *Meas. Sci. Technol.* **27** 084012

Pirnia A, McClure J, Peterson S D, Helenbrook B T and Erath B D 2020 Estimating pressure fields from planar velocity data around immersed bodies; a finite element approach *Exp. Fluids* **61** 55

Ragni D, Ashok A, van Oudheusden B W and Scarano F 2009 Surface pressure and aerodynamic loads determination of a

transonic airfoil based on particle image velocimetry *Meas. Sci. Technol.* **20** 074005

Rendall T C S and Allen C B 2010 Parallel efficient mesh motion using radial basis functions with application to multi-bladed rotors *Int. J. Numer. Methods Eng.* **81** 89–105

Scarano F, Ghaemi S, Caridi G C A, Bosbach J, Dierksheide U and Sciacchitano A 2015 On the use of helium-filled soap bubbles for large-scale tomographic PIV in wind tunnel experiments *Exp. Fluids* **56** 42

Schanz D, Gesemann S and Schröder A 2016 Shake-the-box: Lagrangian particle tracking at high particle image densities *Exp. Fluids* **57** 1–27

Schneiders J F G, Caridi G C A, Sciacchitano A and Scarano F 2016 Large-scale volumetric pressure from tomographic PTV with HFSB tracers *Exp. Fluids* **57** 164

Schneiders J F G and Sciacchitano A 2017 Track benchmarking method for uncertainty quantification of particle tracking velocimetry interpolations *Meas. Sci. Technol.* **28** 065302

Sciacchitano A, Leclaire B and Schröder A 2022 Main results of the analysis of the homer Lagrangian particle tracking and data assimilation database *Proc. 20th Int. Symp. on Application of Laser and Imaging Techniques to Fluid Dynamics* pp 1823–47

Sciacchitano A and Scarano F 2014 Elimination of PIV light reflections via a temporal high pass filter *Meas. Sci. Technol.* **25** 084009

Shams A, Jalalisendi M and Porfiri M 2015 Experiments on the water entry of asymmetric wedges using particle image velocimetry *Phys. Fluids* **27** 027103

Smith M J, Cesnik C E S and Hodges D H 2000 Evaluation of some data transfer algorithms for noncontiguous meshes *J. Aerosp. Eng.* **13** 52–58

Taylor G I and Green A E 1937 Mechanism of the production of small eddies from large ones *Proc. R. Soc.* A **158** 499–521

Thompson J F, Warsi Z U and Mastin C W 1985 *Numerical Grid Generation: Foundations and Applications* (Elsevier North-Holland)

van Gent P L *et al* 2017 Comparative assessment of pressure field reconstructions from particle image velocimetry measurements and Lagrangian particle tracking *Exp. Fluids* **58** 33

Van Gent P 2018 From particles to pressure PIV-based pressure reconstruction for base flows *PhD Thesis* (https://doi.org/10. 4233/uuid:572bc8e5-ffc2-4562-b445-bc061fdc2f00)

van Oudheusden B W 2013 PIV-based pressure measurement *Meas. Sci. Technol.* **24** 032001

Violato D, Moore P and Scarano F 2011 Lagrangian and Eulerian pressure field evaluation of rod-airfoil flow from time-resolved tomographic PIV *Exp. Fluids* **50** 1057–70

Voth G A, Satyanarayan K and Bodenschatz E 1998 Lagrangian acceleration measurements at large Reynolds numbers *Phys. Fluids* **10** 2268–80

Wang C 1990 Exact solutions of the Navier-Stokes equations-the generalized Beltrami flows, review and extension *Acta Mech.* **81** 69–74

Wang J, Zhang C and Katz J 2019 GPU-based, parallel-line, omni-directional integration of measured pressure gradient field to obtain the 3D pressure distribution *Exp. Fluids* **60** 58

Wang Q and Liu X 2023 Green's function integral method for pressure reconstruction from measured pressure gradient and the interpretation of omnidirectional integration *Phys. Fluids* **35** 077113

Westerweel J, Elsinga G E and Adrian R J 2013 Particle image velocimetry for complex and turbulent flows *Annu. Rev. Fluid Mech.* **45** 409–36

Yu F, Gupta N and Hoy J 2005 Non-intrusive pressure measurement based on ultrasonic waves *Insight* **47** 285–8

Zigunov F and Charonko J J 2024 A fast, matrix-based method to perform omnidirectional pressure integration *Meas. Sci. Technol.* **35** 065302